AGU PUBLICATIONS

Geochemistry, Geophysics, Geosystems

RESEARCH ARTICLE
10.1002/2016GC006537

**Key Points:**
- Long-term monitoring of focused vent temperature and chlorinity at the Grotto mound shows significant tidal variations
- The observed tidal variations reflect the poroelastic response of a hydrothermal system to seafloor tidal loading
- Seafloor tidal loading affects hydrothermal venting through subsurface tidal mixing and/or subsurface tidal pumping

**Correspondence to:**
G. Xu,
gxu@whoi.edu

**Citation:**
Xu, G., B. I. Larson, K. G. Bemis, and M. D. Lilley (2017), A preliminary 1-D model investigation of tidal variations of temperature and chlorinity at the Grotto mound, Endeavour Segment, Juan de Fuca Ridge, *Geochem. Geophys. Geosyst.*, *18*, 75–92, doi:10.1002/2016GC006537.

Received 20 JUL 2016
Accepted 9 DEC 2016
Accepted article online 29 DEC 2016
Published online 18 JAN 2017



# A preliminary 1-D model investigation of tidal variations of temperature and chlorinity at the Grotto mound, Endeavour Segment, Juan de Fuca Ridge

**G. Xu[1], B. I. Larson[2], K. G. Bemis[3], and Marvin D. Lilley[4]**

[1]Woods Hole Oceanographic Institution, Woods Hole, Massachusetts, USA, [2]Joint Institute for the Study of the Atmosphere and Ocean, University of Washington, Pacific Marine Environmental Laboratory, NOAA, Seattle, Washington, USA, [3]Department of Marine and Coastal Sciences, Rutgers University, New Brunswick, New Jersey, USA, [4]School of Oceanography, University of Washington, Seattle, Washington, USA

**Abstract** Tidal oscillations of venting temperature and chlorinity have been observed in the long-term time series data recorded by the Benthic and Resistivity Sensors (BARS) at the Grotto mound on the Juan de Fuca Ridge. In this study, we use a one-dimensional two-layer poroelastic model to conduct a preliminary investigation of three hypothetical scenarios in which seafloor tidal loading can modulate the venting temperature and chlorinity at Grotto through the mechanisms of subsurface tidal mixing and/or subsurface tidal pumping. For the first scenario, our results demonstrate that it is unlikely for subsurface tidal mixing to cause coupled tidal oscillations in venting temperature and chlorinity of the observed amplitudes. For the second scenario, the model results suggest that it is plausible that the tidal oscillations in venting temperature and chlorinity are decoupled with the former caused by subsurface tidal pumping and the latter caused by subsurface tidal mixing, although the mixing depth is not well constrained. For the third scenario, our results suggest that it is plausible for subsurface tidal pumping to cause coupled tidal oscillations in venting temperature and chlorinity. In this case, the observed tidal phase lag between venting temperature and chlorinity is close to the poroelastic model prediction if brine storage occurs throughout the upflow zone under the premise that layers 2A and 2B have similar crustal permeabilities. However, the predicted phase lag is poorly constrained if brine storage is limited to layer 2B as would be expected when its crustal permeability is much smaller than that of layer 2A.

## 1. Introduction

Mid-ocean ridge hydrothermal venting is the seafloor manifestation of buoyancy-driven circulation of aqueous fluid within the oceanic crust. Over the past several decades, a large number of studies have observed episodic and periodic variations in long-term monitoring of venting temperature, flow rate, and chemical compositions at both low- and high-temperature hydrothermal systems over a broad range of time scales [e.g., *Little et al*., 1988; *Schultz et al*., 1996; *Sohn et al*., 1998; *Tivey et al*., 2002; *Scheirer et al*., 2006; *Larson et al*., 2007, 2009; *Nees et al*., 2009; *Crone et al*., 2010; *Barreyre et al*., 2014b]. In particular, spectral analysis has identified strong tidal signatures in hydrothermal venting in many of these studies. Among them, some attribute the observed tidal oscillations to the tidally driven bottom currents, which can affect the temperature measured on or just beneath the surface of a hydrothermal sulfide by changing the thickness of the thermal boundary layer [*Little et al*., 1988], advecting warm fluids from adjacent sources [*Tivey et al*., 2002], or through conductive cooling of the sulfide deposit (proposed by *Tivey et al*. [2002] to explain the tidal oscillations observed in the temperature measured by a sensor buried in the sulfide deposit).

Alternatively, other studies interpret observed tidal oscillations, especially in measurements of high-temperature venting made inside the vent chimney, as the poroelastic response of crustal fluids to seafloor tidal loading [e.g., *Larson et al*., 2007, 2009; *Barreyre et al*., 2014b; *Barreyre and Sohn*, 2016]. Based on observations made at the Lucky Strike Hydrothermal Field on the Mid-Atlantic Ridge, *Barreyre et al*. [2014b] suggested that low-temperature venting (i.e., diffuse flows) is mostly affected by bottom currents while high-temperature venting (i.e., "black smokers") is mostly affected by tidal loading. Specifically, two different mechanisms have been proposed to explain how tidal loading can perturb the temperature and chlorinity of high-temperature hydrothermal effluents, which are discussed as follows.

The first mechanism is what we call subsurface tidal mixing. *Larson et al*. [2009] observed tidal oscillations in both venting temperature and chlorinity at multiple high-temperature vents in the Main Endeavour Field (MEF) on the Juan de Fuca Ridge. They interpret those tidal signatures as the result of the tidally driven subsurface mixing between high-chlorinity brine and low-chlorinity vapor. We need to emphasize that the brine and vapor involved in the mixing process discussed in their paper are different from the conjugate brine/vapor pair formed from phase separation of heated seawater within the basal reaction zone of a hydrothermal circulation cell. For the current study, brine and vapor refer broadly to fluids that are enriched and depleted in chloride, respectively, compared to seawater. According to *Fontaine and Wilcock* [2006], as a result of interfacial tensions, rising brine preferentially fills small fissures, dead ends, and backwater porosity thereby covering the inner walls of the main conduits through which vapor flows (Figures 3b and 3c). This is because brine is denser and thus forms a higher density of hydrogen bonds and likely contains a higher proportion of free ions that will enhance the adhesion of brine to rock compared to vapor. Under tidal loading, incremental pore pressure compresses the volume of highly compressible vapor and squeezes the adjacent less-compressible brine into the pore space to fill the void, resulting in the addition of small amounts of brine to vapor-dominated fluid. Such tidally driven mixing causes the temperature and chlorinity of the vapor to vary at tidal frequencies within the subsurface mixing zone. Those variations eventually show up at vent orifices as the vapor reaches the seafloor.

The second mechanism is what we call subsurface tidal pumping. According to *Jupp and Schultz* [2004b], under periodic tidal loading, the varying pore pressure gradient perturbs the flow rate at which hydrothermal fluid ascends along the subsurface discharge zone to oscillate at tidal frequencies. Furthermore, conductive and adiabatic cooling leads to a vertical temperature gradient throughout the discharge zone. As a result, the oscillating flow velocity of ascending hydrothermal fluid causes displacement of the vertical temperature gradient near the seafloor, which then causes the venting temperature to vary at tidal frequencies. As discussed later in this paper, the same mechanism can also lead to tidal oscillations of venting chlorinity assuming a vertical chlorinity gradient is maintained along the discharge zone by diffusion of chloride from brine to vapor.

In this paper, we investigate tidal oscillations observed in time series of venting temperature and chlorinity recorded at the Grotto mound in the MEF from June 2013 to January 2014. We use a one-dimensional two-layer poroelastic model and equations of state applicable to the range of temperature, chlorinity, and pressure within the subsurface hydrothermal discharge zone to test three hypotheses concerning the mechanism for tidal oscillations in focused vents: (1) subsurface tidal mixing causes coupled tidal oscillations in venting temperature and chlorinity [*Larson et al*., 2009], (2) tidal oscillations in temperature and chlorinity are decoupled, with temperature variations originating from subsurface tidal pumping, and chlorinity variations originating from subsurface tidal mixing, and (3) subsurface tidal pumping causes coupled tidal oscillations in venting temperature and chlorinity.

## 2. Study Site

Grotto mound is a large venting sulfide structure (area $\sim$450 $m^2$) within the Main Endeavour Field on the Endeavour Segment of the Juan de Fuca Ridge. Grotto consists of an edifice with NE-SW major axis in the east and a 10 m tall edifice near the western rift valley wall (Figure 1). Grotto is one of the most hydrothermally active structures in the MEF. The elliptical and cylindrical edifices each hosts several "black smokers" with diffuse flows percolating through areas around those smokers. The Grotto mound is also a major study site of the MEF node of the NEPTUNE observatory operated by Ocean Networks Canada. The observatory connects multidisciplinary instruments located on or near Grotto that monitor the local hydrothermal, oceanic, geological, and biological activities [*Kelley et al*., 2014]. Among those instruments, the Benthic and Resistivity Sensors (BARS)—which measure temperature, chlorinity, and oxidation-reduction potential (Eh) inside the throat of a "black smoker" on the elliptical edifice (Figure 1)—is the primary source of the observational data presented in this paper. The contemporaneous seafloor pressure data were recorded by an acoustic Doppler current profiler (ADCP) at approximately 80 m to the south of Grotto.

## 3. Methods

### 3.1. Instrumentation and Data Collection

The BARS instrument package used for this study is detailed in *Larson et al*. [2007] with modifications as described by *Larson* [2008]. The package includes a high-temperature sensor, a resistivity sensor, an Eh

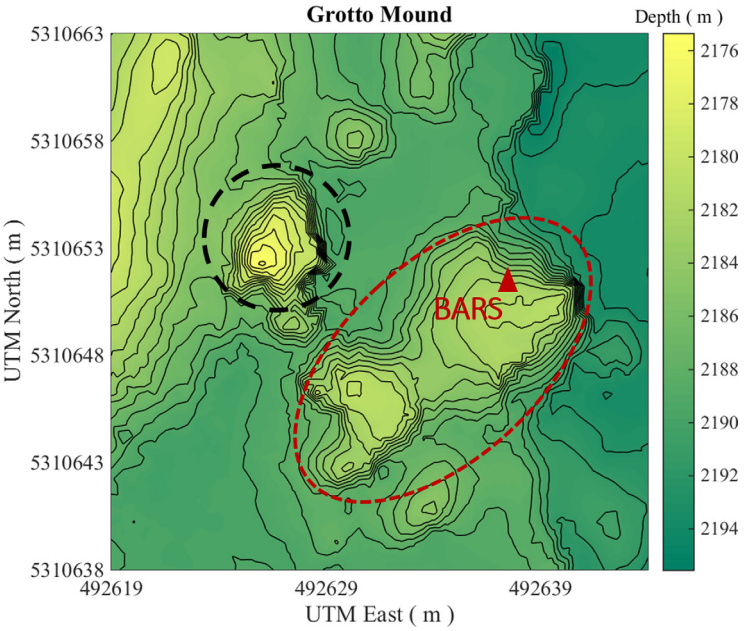


**Figure 1.** Bathymetric map of the Grotto mound. The contour line interval is 1 m. The black and red dashed lines delimit the areas of Grotto's two major edifices, respectively. The red triangle marks the location of the Benthic and Resistivity Sensors (BARS). The bathymetric data used to produce the map were collected during an AUV survey in 2008 with ~1 m lateral resolution and ~0.1 m vertical resolution [*Clague et al*., 2008, 2014].

sensor, and a reference-temperature sensor. The high-temperature, Eh, and resistivity sensors are located at the end of a L-shaped titanium wand with 20 cm after the elbow intended for submersion in a high-temperature sulfide. The reference-temperature sensor is located at the other end of wand in ambient conditions (Figure 2).

The depth of penetration of the high-temperature end can be approximated using grooves in the wand that are spaced approximately 2.5 cm apart. Based on pictures of the deployed wand (Figure 2b), ~5 cm of the back end of the wand is exposed, suggesting ~15 cm of penetration into the sulfide. Pictures taken 11 months after the deployment show the

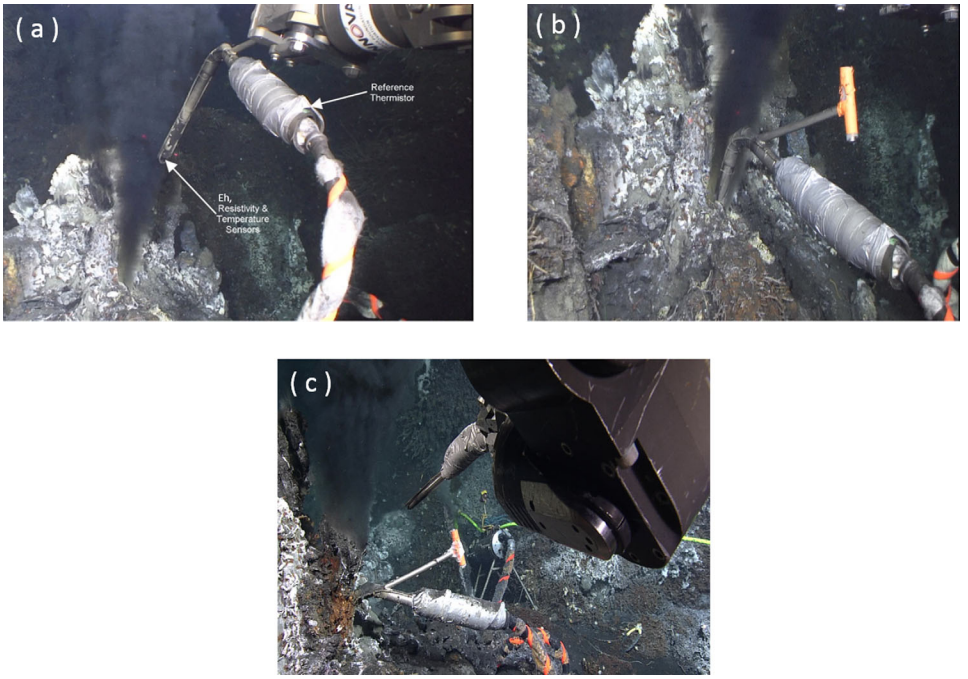


**Figure 2.** (a) Installation of BARS wand into a high-temperature vent at the Grotto mound. The photo was taken on 18 June 2013 at 22:13:06 UTC. The sensor locations are marked in the photo. The reference thermistor is located near the rear end of the L-shaped wand inside the rubber boot covered in duct tape, and the arrow only gives its general location. (b) Close-up view of deployed wand just after installation. Approximately two grooves in the wand are visible, with the third just below the lip of the chimney. The photo was taken approximately 25 min after installation. (c) View of gas tight sampling (top instrument held by the ROV manipulator) in chimney where BARS was deployed 11 months earlier. The photo was taken on 18 May 2014 at 22:21:51 UTC. At this time, the chimney has sealed the entire wand and continued to grow on top of it.

**Table 1.** Sample and Sensor Data for Conductivity-To-Chlorinity Conversion

| Description | Predeployment | During Deployment |
|---|---|---|
| Sample date (UTC) | 18 Jun 2013 (14:57) | 18 May 2014 (22:20) |
| End-member chlorinity (mmol/kg) | 497.5[a] | 435.8 |
| Data used for comparison with sample (UTC) | 18 Jun 2013 (22:55–23:02) | 18 May 2014 (22:21–22:27) |
| Avg. temperature (°C) | 332.7 | 335.6 |
| Avg. conductivity ($V^{-1}$) | 1.41 | 1.51 |

[a]Average of two samples with 1.3% difference.

wand is completely cemented in place up to the elbow, and approximately 10 cm of new chimney has formed on top (Figure 2c). These pictures imply BARS is sensing high-temperature flow that is isolated from the ambient seawater and bottom currents throughout its deployment.

Calibrated temperature values were directly downloaded from Ocean Networks Canada (ONC) database [*Ocean Networks Canada Data Archive*, 2014b], and details of the calibration formula can be found at https://wiki.oceannetworks.ca/display/instruments/15002. For chloride concentrations, resistivity values were first downloaded from the ONC database [*Ocean Networks Canada Data Archive*, 2014a], then the reciprocal taken to give conductivity values in $V^{-1}$ (here and elsewhere, conductivity refers to the inverse of the resistivity measured in volts). Finally, we converted conductivity to chloride concentration using the method described in *Larson et al.* [2007] in conjunction with the Temperature-Conductivity-NaCl surface shown in *Larson* [2008] and average chloride concentration from discrete fluid samples taken prior to and part-way through the BARS deployment (Table 1). The resulting temperature and chlorinity time series have a sampling period of 20 s.

### 3.2. Poroelastic Model

The pressure of the crustal pore fluid hosted by seafloor formations varies in response to tidal loading on the seafloor. Such response includes an instantaneous pore pressure change at all depths and a diffusive pressure change that propagates from the seafloor into the formation and across internal layer boundaries [*Wang and Davis*, 1996; *Jupp and Schultz*, 2004b]. Both instantaneous and diffusive pore pressure variations are dependent on the poroelastic properties of both the pore fluid and the crustal matrix framework. Pore pressure variations are governed by equations of poroelasticity, which have been used in many studies to investigate subseafloor pore pressure variations and their role in fluid flow response to tidal loading and geological events [*Wang and Davis*, 1996; *Davis et al.*, 2000, 2001; *Jupp and Schultz*, 2004b; *Barreyre et al.*, 2014a; *Barreyre and Sohn*, 2016]. In this study, we use the one-dimensional multilayer poroelastic model developed by *Wang and Davis* [1996] to predict the tidally induced pore pressure variations beneath the MEF. Appendix A gives the model equations.

The hydrothermal circulation system consists of a broad recharge zone (presumably primarily on axis), fluid heated at the base of the sheeted dikes just above the axial magma chamber (AMC), and a focused upflow zone [e.g., *Fontaine and Wilcock*, 2006; *Coogan*, 2008; *Coumou et al.*, 2009]. Based on the seismic study of *Van Ark et al.* [2007], the hydrothermal upflow zone beneath the MEF is represented in the model as a poroelastic medium comprising the typical seismic layers 2A and 2B of zero-age oceanic crust (Figure 3). The crustal properties are homogeneous within layers but differ between them. The top boundary of the model is the seafloor, which is open to fluid flow. The bottom boundary of the model is the ceiling of the axial magma chamber (AMC) and is closed to fluid flow. The depths of the layer 2A/2B interface and the AMC are constrained by the seismic observations of *Van Ark et al.* [2007]. Table 2 gives the values of those depths along with other crustal and fluid properties used in the model. Matrix bulk modulus $K_m$, fluid bulk modulus $K_f$, and crustal permeability $k$ are three primary parameters governing the response of the seafloor formation to tidal loading. The matrix bulk modulus $K_m$ is the bulk modulus of the crustal matrix framework when its pore space is empty. In practice, we calculate $K_m$ using Gassmann's equation given in *Jupp and Schultz* [2004b].

Compared with other properties, the crustal permeability $k$ and the fluid bulk modulus $K_f$ are most poorly constrained, particularly the former. For the Endeavour Segment, *Hearn et al.* [2013] estimated the surface permeability to be $k \sim 10^{-11}-10^{-10}\,m^2$ based on high-resolution seafloor photomosaics. Additionally, those authors estimated subsurface permeability to be $k \approx 2.5\times10^{-12}-2\times10^{-10}\,m^2$ for layer 2A and $k \approx 4.0\times10^{-15}-7.9\times10^{-13}\,m^2$ for layer 2B based on a linear relationship between permeability and measured seismic velocity [*Carlson*, 2011; *Newman et al.*, 2011; *Nedimovi et al.*, 2008]. Most recently, *Barreyre and*

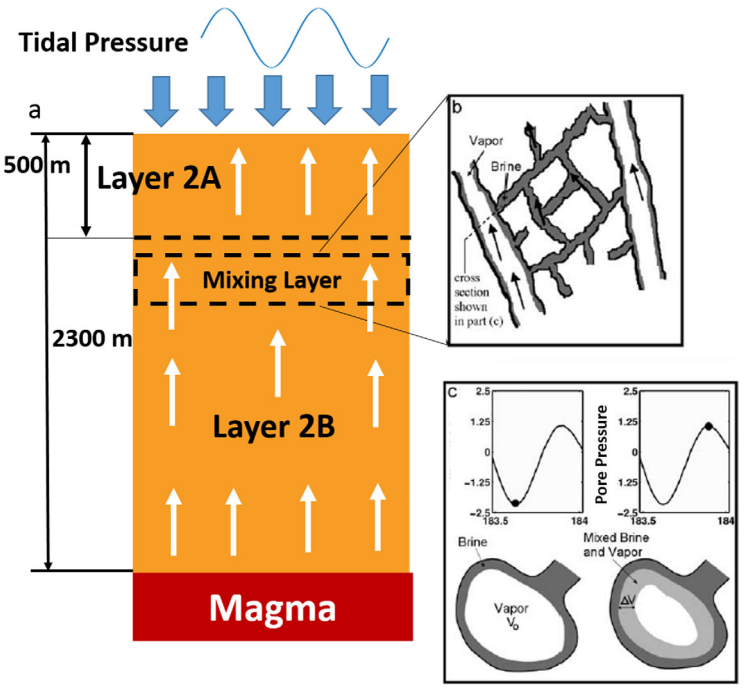


**Figure 3.** (a) Schematic of the crustal structure within the hydrothermal discharge zone in the one-dimensional two-layer poroelastic model. The hypothesized subsurface mixing between brine and vapor occurs within a thin layer beneath the layer 2A/2B interface. (b) Cartoon of brine and vapor distribution within the mixing zone modified from *Fontaine and Wilcock* [2006]. (c) Cartoon illustrating the subsurface mixing between brine and vapor under tidal loading reproduced from *Larson et al.* [2009]. The incremental pore pressure caused by seafloor loading compresses the vapor flowing through a major conduit and squeezes the adjacent less-compressible brine into the void.

*Sohn* [2016] estimated layer 2A permeability at Grotto to be $2.5\times10^{-13}$ m$^2$ based on phase angles of the tidal oscillations in venting temperature and the assumption that subsurface tidal pumping is the causal mechanism for those tidal variations. Alternatively, *Wilcock and McNabb* [1996] and *Lowell et al.* [2013] estimated the uniform crustal permeability to be $k \sim 10^{-13}-10^{-12}$ m$^2$ using mathematical models of hydrothermal convection constrained by observations of the spatial distribution and heat output of hydrothermal venting at Endeavour. Combining the estimates above, we take the ranges of $k$ as: $10^{-13}-10^{-10}$ m$^2$ for layer 2A and $10^{-15}-10^{-12}$ m$^2$ for layer 2B.

The fluid bulk modulus $K_f$ or its reciprocal, compressibility $\beta_f$, is largely determined by fluid temperature $T_f$. Although the venting temperature at Grotto is recorded by BARS at ~332 °C on the seafloor (Figure 4), the subsurface temperature is not as well constrained and can significantly exceed the surface measurements. This is because the temperature of "black smoker" fluid decreases during its ascent as a result of conductive heat loss and adiabatic decompression. *Jupp and Schultz* [2000] and *Jupp and Schultz* [2004a] used a convection model to predict that hydrothermal fluid, constrained by the nonlinear thermodynamic properties of water, may be close to a temperature of 400 °C near the subsurface heat source. In practice, we set $T_f = 370$°C, which is approximately midway between the seafloor temperature measurement (332°C) and the estimated subsurface maximum (400°C). We then calculate the pore fluid compressibility using the equation of state developed by *Driesner* [2007] for 370 °C 2.85 wt % (489 mmol/kg) NaCl solution at a reference pressure of $3.35\times10^4$ kPa. The chlorinity is chosen as the average BARS measurements over a relatively steady period between 10 and 25 October 2013. The reference pressure assumes cold hydrostatic and is calculated at a depth midway between the seafloor and the bottom of the discharge supply conduit.

**Table 2.** Symbols and Values of Parameters

| Symbol | Description | Values and Units |
|---|---|---|
| $k$ | Crustal permeability | m$^2$ |
| $K_f$ | Fluid bulk modulus | Pa |
| $\beta_f$ | Fluid compressibility ($K_f^{-1}$) | Pa$^{-1}$ |
| $K_m$ | Matrix bulk modulus | $6.1\times10^9$ Pa (layer 2A), $4.8\times10^9$ Pa (layer 2B) |
| $S_b$ | Chlorinity of brine | mmol/kg |
| $S_v$ | Chlorinity of vapor | mmol/kg |
| $T_f$ | Temperature of pore fluid | 370°C |
| $T_b$ | Temperature of brine | °C |
| $T_v$ | Temperature of vapor | °C |
| $\phi$ | Crustal porosity [*Crone and Wilcock*, 2005] | 0.2 (layer 2A), 0.03 (layer 2B) |
| $\rho_0$ | Density of cold background pore fluid | 1000 kg/m$^3$ |
| $\rho_v$ | Density of vapor | kg/m$^3$ |
| $\rho_b$ | Density of brine | kg/m$^3$ |
| $\mu$ | Fluid dynamic viscosity | $8.3\times10^{-5}$ Pa · s |
| $\Sigma$ | 1-D storage compressibility | $2.1\times10^{-10}$ Pa$^{-1}$ (layer 2A), $1.5\times10^{-10}$ Pa$^{-1}$ (layer 2B) |
| $\gamma$ | 1-D Skempton ratio | 0.65 (layer 2A), 0.03 (layer 2B) |

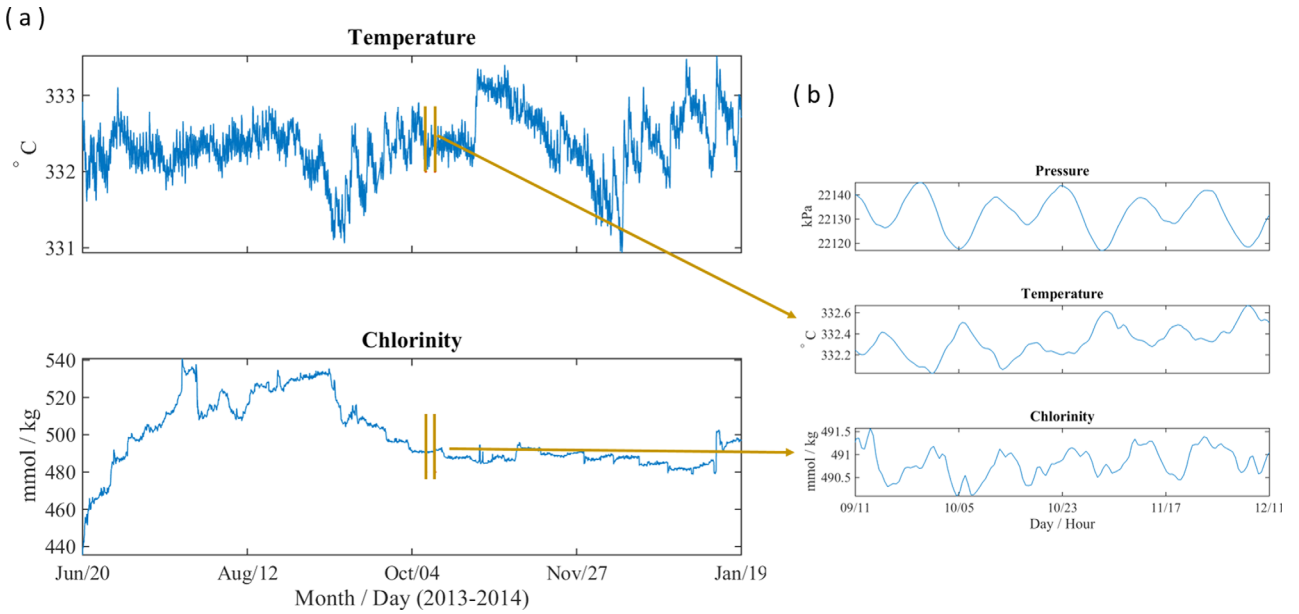


**Figure 4.** (a) Time series of hourly averaged venting (top) temperature and (bottom) chlorinity recorded by BARS at Grotto from June 2013 to January 2014. (b) Zoom-in view of a 3 day period delimited by the vertical lines in Figure 4a of venting (middle) temperature and (bottom) chlorinity along with (top) seafloor pressure measured by the ADCP.

## 4. Results

### 4.1. BARS Data Analysis

Vent temperature and chlorinity data used in this study were recorded by Benthic and Resistivity Sensors (BARS) during its deployment at Grotto between June 2013 and January 2014 (Figure 4). During the 7 month period shown in Figure 4a, temperature fluctuates between 330.5°C and 333.9°C with a mean value of 332°C and a standard deviation of 0.42°C. In comparison, chlorinity shows more pronounced variations, which are from 433 to 544 mmol/kg with a mean value of 500 mmol/kg and a standard deviation of 17.6 mmol/kg. The standard deviation to mean ratio for temperature and chlorinity are 0.1% and 3.5%, respectively. The zoom-in view of a 3 day period from 9 to 12 October 2013 shows periodic oscillations at semidiurnal frequency (twice a day) for both temperature and chlorinity (Figure 4b). Figure 5 shows the power spectra of temperature and chlorinity time series data obtained using the multitaper method [*Thomson*, 1982] with adaptive weighting [*Percival and Walden*, 1993]. The spectrum of temperature has significant peaks within the diurnal and semidiurnal tidal frequency bands with the principal lunar semidiurnal constituent (M2) being the dominant tidal frequency. In comparison, the spectrum of chlorinity has a significant

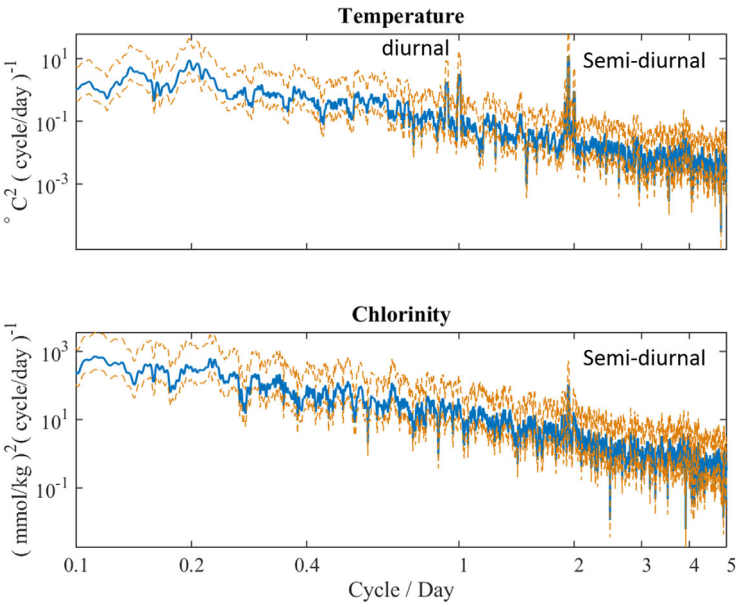


**Figure 5.** (top) Power spectral density of the time series of venting temperature recorded at Grotto between June 2013 and January 2014 (blue). The dashed brown curves delimit the 95% confidence interval. (bottom) Same as top but for chlorinity.

**Table 3.** Harmonic Analysis Results

| | Amplitude | Phase | 1/2 95% CI | Phase Lag With Respect To M2 Tide |
|---|---|---|---|---|
| M2 (semidiurnal) tide | 9 kPa | 241° | 0.28° | 0 |
| Temperature | 0.12°C | 97.1° | 1.82° | 216.1±2.1° |
| Chlorinity | 0.34 mmol/kg | 299.9° | 8.82° | 58.9±9.1° |
| | | | | Phase lag of chlorinity with respect to temperature: 202.8±10.6° |
| K1 (diurnal) tide | 4.3 kPa | 242° | 0.57° | 1±0.85° |
| Temperature | 0.06°C | 77.1° | 7.16° | 195.1±7.73° |
| Chlorinity | 0.2 mmol/kg | 251.9° | 30.86° | 9.9±31.43° |

peak at M2 tidal frequency but shows no indication of the presence of diurnal tidal signals. Given that the dominant tidal constituent in both temperature and chlorinity is M2, we use it as the primary tidal signal for the data analysis described in the rest of the paper. To obtain more details of the M2 tidal oscillations (e.g., amplitude, phase angle, and phase lag relative to tidal pressure), we conducted harmonic analysis on the time series of temperature and chlorinity shown in Figure 4 along with seafloor pressure measured by the ADCP at approximately 80 m to the south of Grotto using the harmonic analysis toolbox T-Tide developed by *Pawlowicz et al*. [2002]. Table 3 shows the results.

Note that the lack of diurnal peak in the spectrum of chlorinity is likely because the amplitude of the diurnal oscillations in chlorinity is small and thus buried in the ambient noise in the spectrum. The formulas given in Appendices A and B suggest the amplitudes of tidal harmonics in temperature and chlorinity should be approximately proportional to the amplitudes of the corresponding loading tides. As shown in Table 3, the amplitude of the diurnal tide (4.3 kPa) is approximately one half of that of the semidiurnal tide (9 kPa). The diurnal harmonic ($K1$) in venting temperature (0.06 °C) is indeed one half of its semidiurnal harmonic (0.12 °C; Table 3). Despite the lack of a visible diurnal peak in the power spectrum, the amplitude of the diurnal harmonic ($K1$) in chlorinity estimated using T-Tide is 0.20 mmol/kg, which is also close to one half of the semidiurnal harmonic (0.34 mmol/kg; Table 3). Therefore, it is likely that subsurface tidal pumping causes chlorinity oscillations at both diurnal and semidiurnal frequencies, and that the former is simply below the noise threshold of the power spectrum.

### 4.2. Subsurface Pore Pressure Variations

We estimate the amplitudes and phase angles associated with the subsurface pore pressure variations under a tidal loading at M2 frequency using the poroelastic model discussed in section 3.2 and Appendix A. Figure 6 shows the result obtained using intermediate crustal permeabilities: $k=5\times10^{-12}$ m$^2$ for layer 2A and $5\times10^{-14}$ m$^2$ for layer 2B and constant fluid compressibility for 370°C 2.85 wt % (489 mmol/kg) NaCl solution at a reference pressure of $3.35\times10^4$ kPa. According to Figure 6, the relative amplitude ($P_r$), which is the ratio of the pore pressure amplitude to the seafloor pressure amplitude, decreases with increasing depth beneath the seafloor. The decrease is minimal within layer 2A (~5% at the interface) due to its large permeability, which leads to fast downward interstitial flow that propagates the seafloor pressure signal through

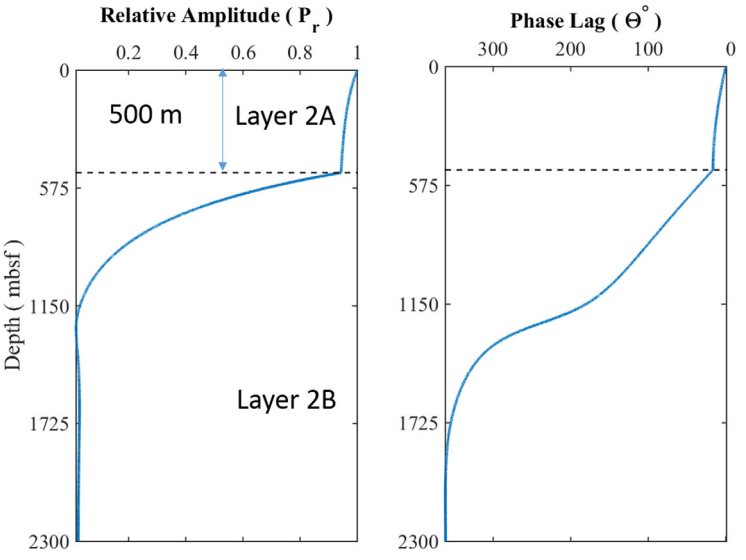


**Figure 6.** (left) Relative amplitude and (right) phase lag of pore pressure oscillations under seafloor loading of M2 tide predicted by the poroelastic model using intermediate crustal permeabilities: $k=5\times10^{-12}$ m$^2$ for layer 2A and $5\times10^{-14}$ m$^2$ for layer 2B and constant fluid compressibility for 370°C 2.85 wt % (489 mmol/kg) NaCl solution at a reference pressure of $3.35\times10^4$ kPa.

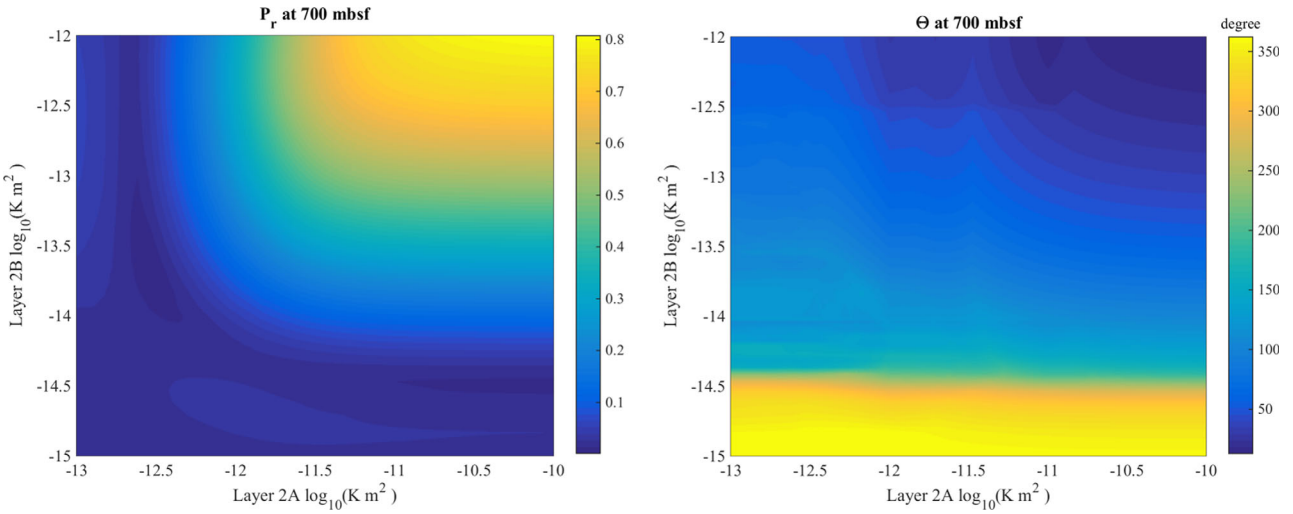


**Figure 7.** Predicted (left) relative amplitude and (right) phase lag of pore pressure oscillations under seafloor loading of M2 tide at 700 mbsf as functions of crustal permeabilities with constant fluid compressibility for 370°C 2.85 wt % (489 mmol/kg) NaCl solution at a reference pressure of $3.35\times10^4$ kPa.

the layer without significant loss of amplitude. Within layer 2B, the relative amplitude decreases exponentially toward a small but nonzero constant—the Skempton ratio, which is the proportion of the seafloor loading that is borne by the pore fluid in the absence of interstitial fluid flows [*Jupp and Schultz*, 2004b]. At 700 mbsf, the value of $P_r$ is 0.39. The phase lag ($\theta$) of the pore pressure variations relative to seafloor loading increases with depth, and the increase is minimal within layer 2A ($\theta \sim 3^\circ$ at the layer 2A/2B interface). Such a small phase lag is also due to the large permeability of layer 2A and the resulting fast interstitial flow that propagates the seafloor pressure signal through the layer without much delay. Within layer 2B, $\theta$ increases rapidly, reaching 360° (zero) by a depth of 1800 m with the permeability and fluid compressibility used. At 700 mbsf, the phase lag is $\theta=64^\circ$. Figure 7 shows the variations of $P_r$ and $\theta$ at 700 mbsf as functions of layers 2A and 2B permeabilities. According to Figure 7, $P_r$ increases with increasing permeabilities of both layers and is more sensitive to the permeability of layer 2B. In contrast, $\theta$ decreases with increasing permeabilities of both layers and is also more sensitive to the permeability of layer 2B.

### 4.3. Coupled Tidal Oscillations of Temperature and Chlorinity From Subsurface Tidal Mixing

As hypothesized by *Larson et al*. [2009], the tidal oscillations in venting temperature and chloride may originate from the subsurface tidal mixing between brine and vapor at depths where the vapor is close to its critical point and thus highly compressible. In order to test this hypothesis, we estimate the brine temperature and chlorinity and vapor compressibility needed to generate temperature and chlorinity oscillations of the observed amplitudes.

For modeling purposes, we assume the chlorinity of the vapor to be $S_v=S_0-A_s=488.5$ mmol/kg or 2.85 wt %, where $S_0=488.8$ mmol/kg is the time average of the chlorinity recorded over a relatively steady period from 10 to 25 October 2013 (Figure 4) and $A_S \approx 0.3$ mmol/kg is the amplitude of the M2 tidal oscillations in chlorinity (Table 3). The corresponding critical temperature and pressure of a NaCl solution with the same chlorinity are ~400 °C and $\sim2.9\times10^4$ kPa, respectively [*Driesner and Heinrich*, 2007]. The critical pressure corresponds to approximately 700 m beneath the MEF, which is thus assumed to be the primary depth at which the subsurface mixing occurs. In addition, we also assume the temperature of the near-critical vapor to be 400°C. Note that this is different from the vapor temperature used in the poroelastic model (370°C) as the latter is considered the average over the discharge zone and hence more suitable to use in the model that assumes constant fluid properties.

As mentioned in section 1, the increased pore pressure under tidal loading compresses the volume filled by the highly compressible near-critical vapor and squeezes the adjacent brine into the pore space to fill in the void. We can then estimate the volume fraction of brine ($\eta_b$) and vapor ($\eta_v$) in the mixing process as

$$\eta_b = \Delta P \beta_f, \tag{1}$$

where $\Delta P$ is the incremental pore pressure and $\beta_f$ is the compressibility of the near-critical vapor. In practice, we determine $\Delta P$ as the product of the relative amplitude of pore pressure oscillations ($P_r$) predicted by the poroelastic model (Figure 7) and the amplitude of the M2 oscillations in seafloor pressure estimated from harmonic analysis ($A_P$=9 kPa, Table 3). In addition, we assume $\beta_f$ to vary from $10^{-7}$ to $10^{-6}$ $Pa^{-1}$. The purpose of using this arbitrary range, which is independent of vapor temperature (400°C), is to obtain a hypothetical minimum vapor compressibility that is required to explain the observed tidal oscillations of temperature and chlorinity as discussed in the following.

Assuming mass, heat, and chloride are conserved during mixing leads to the following equations

$$\eta_v \rho_v + \eta_b \rho_b = \epsilon \rho_m, \tag{2}$$

$$\chi_v H_v + \chi_b H_b = H_m. \tag{3}$$

$$\chi_v S_v + \chi_b S_b = S_m, \tag{4}$$

Equation (2) represents the conservation of mass, where $\rho$ is the fluid density and the subscripts $v$, $b$, and $m$ refer to vapor, brine, and mixture, respectively; $\epsilon$ is a constant coefficient used to compensate for the non-conserved nature of fluid volume during mixing. From equation (2), we derive the mass fractions of vapor and brine as $\chi_v = (\eta_v \rho_v)/(\epsilon \rho_m)$ and $\chi_b = 1 - \chi_v$. Equations (3) and (4) represent the conservation of heat and chloride, respectively, where $H$ and $S$ are enthalpy and chlorinity.

In general, one can solve equations (2–4) to obtain the temperature and chlorinity of brine using the temperatures and chlorinities of vapor and mixture along with the formulas to calculate enthalpy and density as functions of temperature, chlorinity, and pressure. In our modeling, we determine the temperatures and chlorinities of vapor and mixture as follows. First, we assume the mixture is a result of colder brine mixing with hotter vapor. As discussed in the beginning paragraph of this section, we assume the temperature and chlorinity of vapor to be $T_v$=400 °C and $S_v$=448.5 mmol/kg. We then determine the temperature of mixture as $T_m = T_v - 2A_T$=399.8 °C where $A_T \approx 0.1$ °C is the amplitude of the M2 tidal oscillations in temperature (Table 3). Similarly, we determine the chlorinity of mixture as $S_m = S_v + 2A_S$=449.1 mmol/kg. Additionally, we use the formulas given in *Driesner* [2007] to calculate vapor and mixture enthalpy and density as functions of temperature and chlorinity at $2.9 \times 10^4$ kPa. After obtaining brine enthalpy by solving equations (2–4), we convert it to brine temperature inversely based on the enthalpy formula given in *Driesner* [2007].

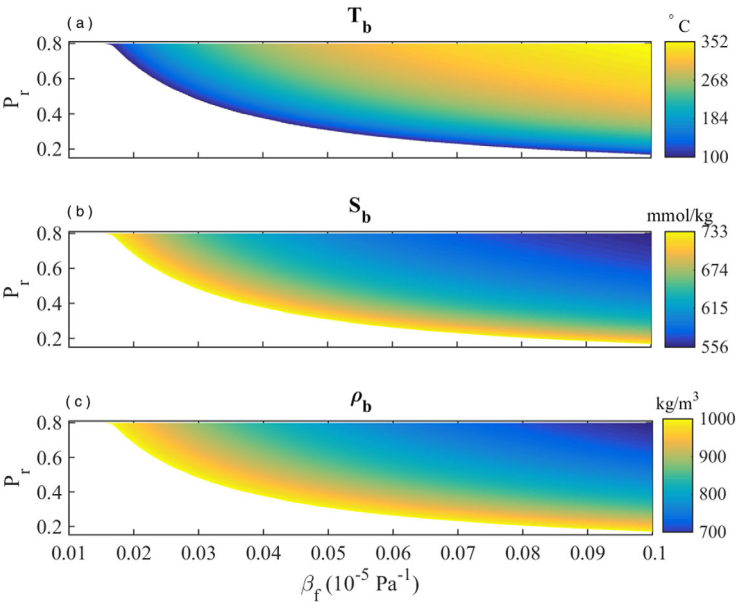


**Figure 8.** Estimated brine properties from coupled temperature and chlorinity tidally oscillations caused by subsurface tidal mixing: (top) temperature, (middle) chlorinity, and (bottom) density as functions of vapor compressibility ($\beta_f$) and relative amplitude of pore pressure oscillations ($P_r$). The results are cropped at the presumed maximum brine density of 1000 kg/m$^3$.

Figure 8 shows the temperature ($T_b$), chlorinity ($S_b$), and density ($\rho_b$) of brine obtained with vapor compressibility ($\beta_f$) varying from $10^{-7}$ to $10^{-6}$ $Pa^{-1}$ and $P_r$= 0.1 to 0.8. The lower limit of $P_r$ correspond to the pore pressure variations at 700 mbsf predicted by the poroelastic model with crustal permeabilities of $K = 8.1 \times 10^{-12}$ m$^2$ for layer 2A and $K = 8.6 \times 10^{-15}$ m$^2$ for layer 2B. The upper limit of $P_r$ corresponds to $K = 9.1 \times 10^{-11}$ m$^2$ for layer 2A and $K = 9.1 \times 10^{-13}$ m$^2$ for layer 2B. According to Figure 8, at

fixed $P_r$, $T_b$ increases with increasing $\beta_f$ while $S_b$ and $\rho_b$ follow the opposite trend. At fixed $\beta_f$, $T_b$ increases with increasing $P_r$ and the opposite applies to $S_b$ and $\rho_b$. Also, notice the cutoff of brine density at $\rho_b$=1000 kg/m$^3$. Such a cutoff density is chosen based on the assumption that the pressure gradient within the lower hydrothermal discharge zone in layer 2B is close to cold hydrostatic [*Jupp and Schultz*, 2004a; *Fontaine and Wilcock*, 2006] and thus only brines with density lower than that of the cold pore fluid (~1000 kg/m$^3$) will rise from the basal reaction zone and reach 700 mbsf. Consequently, Figure 8 suggests the minimum vapor compressibility required to interpret the tidal oscillations of temperature and chlorinity is $\beta_f$=1.9×10$^{-7}$ Pa$^{-1}$ at $P_r$=0.8. This minimum increases to $\beta_f$=10$^{-6}$ Pa$^{-1}$ at $P_r$=0.14.

### 4.4. Decoupled Tidal Oscillations of Temperature and Chlorinity

The results shown in section 4.3 are obtained based on the premise that subsurface tidal mixing causes the tidal oscillations in both venting temperature and chloride. Alternatively, it is plausible that the tidal signatures in temperature and chloride are decoupled and originate from separate causal mechanisms. For example, as discussed in section 1, subsurface tidal pumping can be an alternative causal mechanism for the tidal oscillations observed in venting temperature.

To test the hypothesis that subsurface tidal mixing causes the tidal oscillations in venting chlorinity alone, we redo the calculations described in section 4.3 by solving equations (2–4) under the condition of $T_v$=$T_b$ for mixing between brine and vapor in thermal equilibrium. We also assume subsurface mixing remains restricted to 700 mbsf. Figure 9 shows estimated brine chlorinity ($S_b$) and density ($\rho_b$) varying as functions of vapor temperature ($T_v$) and compressibility ($\beta_f$) at varying relative amplitude of pore pressure oscillations ($P_r$=0.1 to 0.8). At fixed $P_r$, both $S_b$ and $\rho_b$ decrease with increasing $T_v$ and hence $\beta_f$. Furthermore, $S_b$ and $\rho_b$ decrease with increasing $P_r$ at fixed $T_v$ and $\beta_f$. Note that the results are clipped at $\rho_b$=1000 kg/m$^3$, which is the presumed maximum density of the rising brine within the discharge zone (see discussion in section 4.3).

According to Figure 9, the brine properties required to explain the tidal oscillations in chloride are $T_b$=380 to 400 °C and $S_b$=6485 – 2280 mmol/kg. Note that the maximum of $S_b$ is within the range of the model predicted chlorinity (30–50 wt % or 5133–8556 mmol/kg) of the end-member brine formed in the basal reaction zone [*Choi and Lowell*, 2015], which suggests minimal alteration of the end-member brine after it leaves its point of origin. On the other hand, the lower values of $S_b$ point to dilution of the end-member brine by less-saline pore fluids during ascent and prior to tidally driven mixing with vapor.

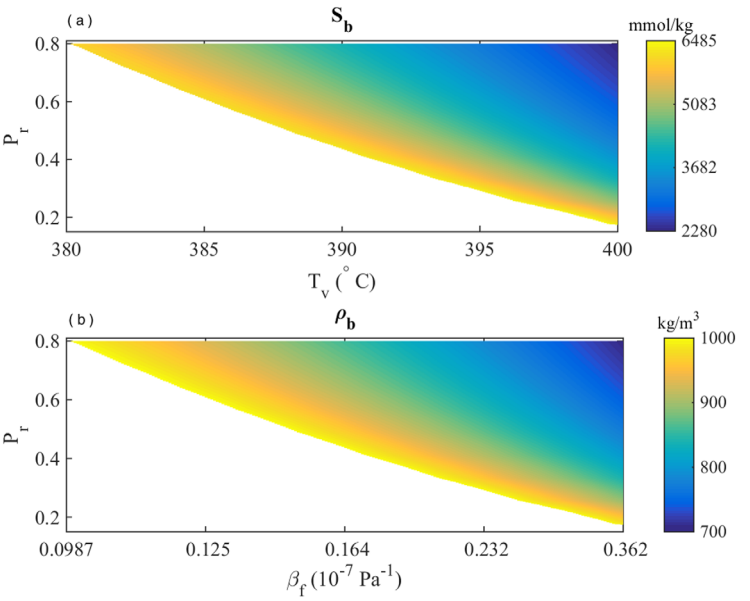


**Figure 9.** Estimated brine properties from decoupled temperature and chlorinity tidal oscillations: (top) chlorinity and (bottom) density as functions of vapor temperature ($T_v$)/compressibility ($\beta_f$) and relative amplitude of pore pressure oscillations ($P_r$). The results are cropped at the presumed maximum brine density of 1000 kg/m$^3$.

### 4.5. Coupled Tidal Oscillations of Temperature and Chlorinity From Subsurface Tidal Pumping

The conceptual model of the storage of brine within the discharge zone of a hydrothermal circulation cell (whereby brine preferentially fills small fissures, dead ends, and covers the inner walls of the main conduit through which the vapor flows [*Fontaine and Wilcock*, 2006]) should allow another explanation for the tidal oscillations in venting chlorinity. As illustrated in Figure 10, if the inner walls of the main conduits through which the vapor rises are covered by brine, then chloride will be transferred from brine to vapor through

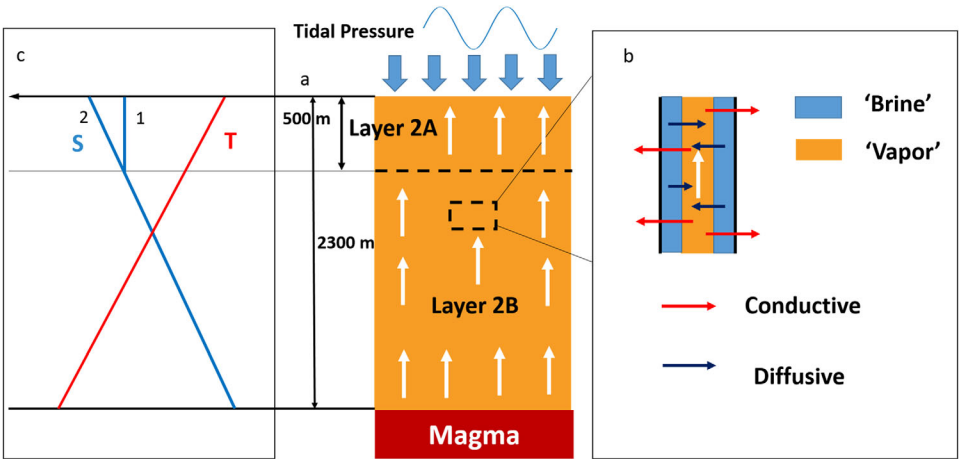


**Figure 10.** Schematic of the formation of temperature and chlorinity gradients along the hydrothermal discharge zone. The temperature gradient forms as a result of the conductive and adiabatic cooling of the rising vapor. The chlorinity gradient forms as a result of the diffusion of chloride from brine to vapor within the major conduits. Unlike the temperature gradient that persists throughout the discharge zone, the chlorinity gradient may end at the layer 2A/2B interface because of the absence of brine storage in layer 2A when the crustal permeability of layer 2A is much larger than that of layer 2B (case 1). Alternatively, the chlorinity gradient can persist throughout the discharge zone as the temperature gradient when the crustal permeability of layer 2A is similar to that of layer 2B (case 2).

diffusion. Such diffusion will cause the chlorinity of a vapor parcel rising through the conduit to increase gradually and thus leads to a vertical chlorinity gradient along the discharge zone. Unlike the vertical temperature gradient caused by conductive and adiabatic heat loss, which can persist through out the discharge zone, the chlorinity gradient may only exist within layer 2B assuming a permeability contrast between layers 2A and 2B. According to *Fontaine and Wilcock* [2006], when layer 2A has much larger permeability than layer 2B, the vertical pressure gradient driving the upflow in layer 2A is much smaller than the pressure gradient in layer 2B. As a result, the rising brine becomes negatively buoyant after it crosses the interface and ultimately starts sinking. In this case, the storage of brine occurs only in layer 2B such that the vertical gradient of "vapor" chlorinity does not extend beyond the 2A/2B contrast (Figure 10c2). Alternatively, when layers 2A and 2B have comparable permeabilities, the storage of brine will persist through out the discharge zone as will the vertical gradient of vapor chlorinity (Figure 10c1).

If vertical temperature and chlorinity gradients exist along the discharge zone, then *the mechanism of subsurface tidal pumping can lead to coupled tidal oscillations in venting temperature and chlorinity*. Under tidal loading, the flow rate of the rising vapor will oscillate at tidal frequencies driven by the oscillating pore pressure gradient. Such oscillating flow velocity causes displacement of the vertical temperature and chlorinity gradients, which then causes the temperature and chlorinity of the vapor at a given depth to vary at tidal frequencies. Theoretically, we can estimate the phase lag of temperature relative to tidal loading at the seafloor from the pore pressure variations predicted by the two-layer poroelastic model (section 4.2) using the formulas adapted from the ones given in *Jupp and Schultz* [2004b] (Appendix B). According to Figure 11, for M2 tide, the phase lag of venting temperature decreases with increasing layer 2A permeability and is relatively insensitive to layer 2B permeability. The layer 2A permeability corresponding to the observed phase lag has a mean value of $1.5\times10^{-12}$ m$^2$ (contour lines in Figure 11). Note that this estimate is approximately 1 order of magnitude higher than that obtained by *Barreyre and Sohn* [2016] ($2.5\times10^{-13}$ m$^2$) based on the single-layer simplification of the poroelstic formulas given in Appendices A and B. In their model, the impermeable bottom boundary is set at the layer 2A/2B interface, which is essentially comparable to our two-layer model with very small layer 2B crustal permeability (i.e., the lower ends of the contour lines in Figure 11). The discrepancy is due to the large difference between the fluid compressibility applied. In the current study, the fluid compressibility is calculated using the equation of state developed by *Driesner* [2007] for 370°C 2.85 wt % (489 mmol/kg) NaCl solution at a reference pressure of $3.35\times10^4$ kPa. The result: $\beta_f=5.3\times10^{-9}$ Pa$^{-1}$ is an order of magnitude higher than the one used by *Barreyre and Sohn* [2016]: $\beta_f=4.8\times10^{-10}$ Pa$^{-1}$, which is relatively low for high-temperature pore fluids.

For venting chlorinity, when layer 2A/2B have comparable permeabilities (close to the upper ends of the contour lines in Figure 11), the storage of brine and thus the vertical gradient of vapor chlorinity are expected to persist throughout the discharge zone. In this case, we can estimate the phase lag of venting

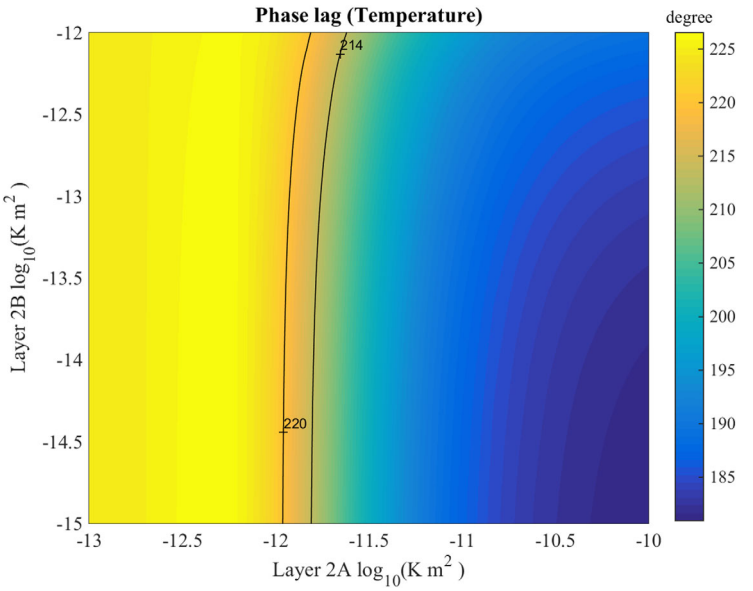


**Figure 11.** Phase lag of venting temperature relative to M2 tide predicted by the poroelastic model. The contours lines mark the lower and upper limit of the observed phase lag.

chlorinity in the same manner as temperature (see Appendix B for the formulas used). The results suggest venting chlorinity is essentially out of phase (i.e., lagging by 180° with deviation $<0.15°$) with venting temperature across the entire range of the layer 2A/2B crustal permeabilities applied, which is expected because the vertical gradients of chlorinity and temperature have opposite signs with temperature increasing and chlorinity decreasing with depth. This prediction is also close to the observed phase lag between venting chlorinity and temperature: $204\pm16°$ (Table 3).

When layer 2A has much larger permeability than layer 2B (close to the lower ends of the contour lines in Figure 11), the storage of brine only occurs in layer 2B and the vertical gradient of vapor ends at the layer interface (Figure 10c2). As a result, the tidal phase of chlorinity observed at the seafloor should be the tidal phase at the interface plus what is associated with the time taken by the vapor to reach the seafloor or the residence time of high-temperature hydrothermal fluid in layer 2A. The latter is dependent on the interstitial upflow velocity within layer 2A. In this study, we assume the upflow velocity is uniform throughout the discharge zone and obtain an estimate as (Appendix B):

$$w=\frac{Q}{\rho_v A\phi}, \tag{5}$$

where $w$ is the interstitial upflow velocity, $Q=292$ kg/s is the estimated mass flux within the discharge zone beneath the MEF [*Lowell et al*., 2013], $\rho_v=646$ kg/m$^3$ is the vapor density, $A$ is the area of the horizontal cross section of the upper discharge zone in layer 2A, which is assumed to equal the area of the vent field: $6\times10^4$ m$^2$ [*Lowell et al*., 2013], and $\phi=0.2$ is the crustal porosity of layer 2A [*Crone and Wilcock*, 2005]. The result: $w=3.8\times10^{-5}$ m/s suggests that it will take approximately 154 days for the vapor to rise through the 500 m thick layer 2A. Such a residence time is likely an overestimate since $w$ is calculated assuming the area of the horizontal cross section of the discharge zone in layer 2A equals the area of the entire vent field. In order to shorten the residence time to the period of M2 tide ($\sim$0.5 day), the area of the horizontal cross section of the discharge zone needs to be smaller than 1% of the area of the vent field. Either way, the tidal phase of venting chlorinity is poorly constrained because of the large uncertainty in the upflow residence time in layer 2A.

## 5. Discussion

### 5.1. Hypothesis Test Results

As for the first hypothesis, according to the discussion in section 4.3, interpreting the observed tidal oscillations in temperature and chloride as a result of subsurface mixing alone requires the vapor to be highly compressible: $\beta_f > 1.9\times10^{-7}$ Pa$^{-1}$. This lower limit of $\beta_f$ is within the range of the estimated $\beta_f$ for near-critical water [*Johnson and Norton*, 1991], whose compressibility goes to infinity at its critical point. However, for a NaCl solution, the maximum compressibility is finite and decreases dramatically with increasing chlorinity. According to *Klyukin et al*. [2016], the maximum of $\beta_f$ for a NaCl solution with the same chlorinity as

the vapor (2.85 wt %) is $6.7\times10^{-8}$ $Pa^{-1}$, which is approximately a third of the minimum compressibility required to explain the coupled temperature and chloride tidal oscillations. In addition, according to Figure 8a, the estimated brine temperature is at least 48°C lower than the vapor temperature (400°C). It is questionable such a sharp thermal gradient can exist given the close proximity between brine and vapor in the hypothesized subseafloor layout (Figure 3), whereby thermal conduction is likely to homogenize any temperature difference and lead to thermal equilibrium between brine and vapor. The arguments above thus invalidate the first hypothesis, which is subsurface tidal mixing causes coupled tidal oscillations in venting temperature and chlorinity.

As for the second hypothesis, comparing the results shown in Figure 9 with Figure 8, the requirement for highly compressible near-critical vapor is relaxed in the case of decoupled temperature and chlorinity oscillations. The minimum compressibility required to explain chloride oscillations alone is $\beta_f \sim 1\times10^{-8}$ $Pa^{-1}$ at $P_r=0.8$. This minimum increases to $4\times10^{-8}$ $Pa^{-1}$ at $P_r=0.14$. Those values are both below the estimated maximum compressibility of $6.7\times10^{-8}$ $Pa^{-1}$ for near-critical vapor [*Klyukin et al*., 2016]. As a result, when $P_r$ is high, which corresponds to large crustal permeabilities (e.g., $P_r=0.8$ corresponds to $K=9.1\times10^{-11}$ $m^2$ for layer 2A and $K=9.1\times10^{-13}$ $m^2$ for layer 2B), the requirement for near-critical vapor is lifted and thus the mixing is no-longer restricted to the depth corresponding to the critical pressure of the vapor (e.g., $2.9\times10^4$ kPa). Therefore, instead of being limited to a thin vertical layer, as presumed in deriving the results shown in Figure 9, the mixing process can occur over a relative broad segment of the discharge zone where brine is stored and the tidally driven subsurface pore pressure change is significant.

As for the third hypothesis, that subsurface tidal pumping causes coupled tidal oscillations in venting temperature and chlorinity, the results shown in section 4.5 suggest, as predicted by the poroelastic model, the phase angle of the M2 tidal oscillations in venting temperature correspond to the layer 2A crustal permeability of $\sim1.5\times10^{-12}$ $m^2$. This value falls into the range of the previous estimates ($10^{-10}$ to $10^{-13}$ $m^2$). In addition, the phase lag between the tidal oscillations in temperature and chlorinity predicted by the poroelastic model (~180°) is close to the observation (204±16°) in the case of layers 2A and 2B having similar permeabilities. When the permeability of layer 2A is much larger than that of layer 2B, the phase lag is poorly constrained.

In summary, the discussion above suggests the first hypothesis is unlikely to be the causal mechanism for the tidal oscillations of hydrothermal venting at Grotto, while the second and third hypotheses can both potentially explain the observation. The current model prediction and observational data are inadequate to determine which one is the dominant mechanism.

### 5.2. Limitations of 1-D Poroelastic Model

In this study, the one-dimensional poroelastic model used to estimate the incremental pore pressure assumes single-phase fluid (vapor) with uniform properties. In reality, the presence of brine and spatial variations of fluid properties will introduce additional uncertainty into the pore pressure predicted by the model. In addition, since the model is one dimensional, it excludes lateral pressure gradients and interstitial flows. However, 2-D numerical simulations suggest tidal loading can result in lateral pressure gradients that drive horizontal flows into and out of the discharge zone of a hydrothermal circulation cell [*Crone and Wilcock*, 2005]. The horizontal pressure gradient is a result of the lateral contrast of crustal and pore fluid properties across the interface between the focused hydrothermal discharge zone and its host formation. Those different crustal and fluid properties lead to different poroelastic response to tidal loading and hence lateral pore pressure gradient and interstitial flows across the interface. The presence of horizontal flows into and out of the discharge zone causes its pore pressure and vertical interstitial flow variations to deviate from those predicted by the 1-D model and thus introduces additional uncertainty into the results presented in this paper. More importantly, the tidally driven horizontal interstitial flows can drive mixing of pore fluids with contrasting temperature and chlorinity between the discharge zone and its surroundings, which, by itself, can potentially result in the observed tidal variations of venting temperature and chlorinity. To test this hypothesis and better understand subsurface fluid flows and their influences on seafloor venting requires developing a 2-D poroelastic model with both two-phase fluids [*Choi and Lowell*, 2015] and seafloor tidal loading [*Crone and Wilcock*, 2005] that accounts for the lateral heterogeneity of crustal and fluid properties, which will be a goal for future research.

## 6. Conclusions

This study tests three hypothetical scenarios in which seafloor pressure loading can lead to tidal modulations of venting temperature and chlorinity at the Grotto mound through subsurface tidal mixing and/or subsurface tidal pumping. The results suggest it is unlikely for subsurface tidal mixing to cause coupled tidal oscillations of the observed amplitudes in venting temperature and chlorinity. It is possible that the tidal oscillations in venting temperature and chlorinity are decoupled with subsurface tidal pumping causing the temperature variations and subsurface tidal mixing causing the chlorinity variations, although the mixing depth is not well constrained. Finally, it is plausible for subsurface tidal pumping to cause coupled tidal oscillations in venting temperature and chlorinity. In this case, the observed tidal phase lag between venting temperature and chlorinity is close to the poroelastic model prediction if the brine storage occurs throughout the upflow zone under the premise that layers 2A and 2B have similar crustal permeabilities. On the other hand, the phase lag is poorly constrained if the brine storage is limited to layer 2B when its crustal permeability is much smaller than that of layer 2A. Last but not least, the results summarized above are preliminary due to the complexity of subseafloor hydrothermal circulation that is unaccounted for by the simplified 1-D poroelastic model applied. Likewise, the analysis in this paper is insufficient to rule out other mechanisms, such as lateral mixing of pore fluid between discharge zone and surroundings (section 5.2), as the cause of the observed tidal signals in venting temperature and chlorinity. A more realistic way to investigate the poroelastic response of hydrothermal circulation to tidal loading and a goal for future research will be to develop a 2-D poroelastic model with two-phase fluids and seafloor loading.

## Appendix A: Two-Layer Poroelastic Model Formulas

According to the theory of poroelasticity, under seafloor tidal loading, the pore pressure perturbation ($\hat{P}$) comprises an instantaneous component ($\hat{P}_i$) that is invariant with depth and a flow-induced diffusive component ($\hat{P}_d$) that propagates from the seafloor into the crustal formation and from the formation layer interfaces into internal layers [*Wang and Davis*, 1996; *Jupp and Schultz*, 2004b]. Between the two components, $\hat{P}_i$ is in phase with the loading tide while $\hat{P}_d$ is lagging with a phase angle dependent on the tidal period along with crustal and fluid properties.

According to *Wang and Davis* [1996], the pore pressure perturbation within each layer of the one-dimensional crustal formation illustrated in Figure 3 is governed by the following equation:

$$\frac{\partial \hat{P}_j}{\partial t} - \frac{k_j}{\mu_j \Sigma_j}\frac{\partial^2 \hat{P}_j}{\partial z^2} = \gamma_j \frac{\partial \sigma_P}{\partial t}, \tag{A1}$$

where the subscript $j$ denotes properties in layer 2A: $j=1$ and layer 2B: $j=2$, $\mu$ is dynamic viscosity, $\Sigma$ and $\gamma$ are the one-dimensional storage compressibility and Skempton ratio, respectively [*Jupp and Schultz*, 2004b], and $\sigma_P = A_P \exp(i\Omega t)$ is the loading tidal harmonic having amplitude $A_P$ and angular frequency $\Omega$. In practice, we estimate dynamic viscosity as a function of fluid temperature as $\mu = C_1/(C_2 + T_f)$, where $T_f = 370^\circ$C, $C_1 = 0.032$ Pa s/$^\circ$C, and $C_2 = 15.4^\circ$C [*Germanovich et al.*, 2000]. We calculate $\Sigma$ and $\gamma$ using the formulas given in *Jupp and Schultz* [2004b] and the typical values of layer 2A/2B crustal properties given in *Crone and Wilcock* [2005]. The solution to equation (A1) can be decoupled into instantaneous and diffusive components

$$\hat{P}_j = \hat{P}_{ij} + \hat{P}_{dj}, \tag{A2}$$

which satisfy the governing equations [*Wang and Davis*, 1996]

$$\hat{P}_{ij} = \gamma_j \sigma_P, \tag{A3}$$

$$\frac{\partial \hat{P}_{dj}}{\partial t} = \frac{k_j}{\mu_j \Sigma_j}\frac{\partial^2 \hat{P}_{dj}}{\partial z^2}. \tag{A4}$$

In practice, equation (A4) is solved with the following boundary conditions. First, the seafloor is treated as an open boundary for fluid flow and thus at $z = 0$ m,

$$\hat{P}_1 = \hat{P}_{i1} + \hat{P}_{d1} = \sigma_P. \tag{A5}$$

At layer 2A/2B interface ($z=-h=-500$ m), the continuity of pore pressure and Darcy fluid velocity requires

$$\hat{P}_{d1}+\gamma_1\sigma_P=\hat{P}_{d2}+\gamma_2\sigma_P, \tag{A6}$$

$$\frac{k_1}{\mu_1}\frac{\partial\hat{P}_{d1}}{\partial z}=\frac{k_2}{\mu_2}\frac{\partial\hat{P}_{d2}}{\partial z}. \tag{A7}$$

The bottom boundary of layer 2B is treated as impermeable to fluid flows and thus at $z=-H=-2300$ m

$$\frac{k_2}{\mu_2}\frac{\partial\hat{P}_{d2}}{\partial z}=0. \tag{A8}$$

Assuming the solution to equation (A4) has the following form

$$\hat{P}_{dj}=C_j(z)\exp(i\Omega t), \tag{A9}$$

substituting into equation (A4) gives

$$i\Omega C_j=\frac{k_j}{\mu_j\Sigma_j}\frac{\partial^2 C_j}{\partial z^2}. \tag{A10}$$

The solution to equation (A10) has the form

$$C_j(z)=a_j\exp(\Psi_j z)+b_j\exp(-\Psi_j z), \tag{A11}$$

where $\Psi=\sqrt{i\Omega\mu_j\Sigma_j/k_j}$ and $a_j$, $b_j$ are constant coefficients. Substituting (A11) into the boundary conditions (A5)–(A8) leads to a system of four equations that is solved for $a_1$, $b_1$, $a_2$, $b_2$. The values of the constant parameters used are given in Table 2.

## Appendix B: Temperature and Chlorinity Variations From Subsurface Tidal Pumping

This section gives the formulas used to calculate the phase lags of venting temperature and chlorinity relative to ocean tide from the pore pressure variations predicted by the poroelastic model described in Appendix A. As discussed in section 4.5, the conductive and adiabatic cooling causes the temperature of vapor to decrease as it rises through the subsurface discharge zone. In the meantime, the chlorinity of vapor increases as a result of the diffusion of chloride from brine to vapor inside a major conduit (Figure 10). We thus assume the steady state vapor temperature and chlorinity to be

$$\bar{T}_v=\bar{T}_{v0}-\Gamma_T z, \tag{B1}$$

$$\bar{S}_v=\bar{S}_{v0}+\Gamma_S z. \tag{B2}$$

where $T_{v0}$ and $S_{v0}$ are the steady state temperature and chlorinity at the seafloor; $\Gamma_T$ and $\Gamma_S$, both of which are positive constants, are the steady state gradients.

Assuming thermal equilibrium between the rising vapor and the bounding rock, then the steady state vertical advection speed for temperature signals can be estimated as

$$\bar{w}_T=\frac{Q}{\rho_v A}, \tag{B3}$$

where $Q=292$ kg/s is the estimated mass flux within the discharge zone beneath the MEF [*Lowell et al.*, 2013], $\rho_v=646\,\mathrm{kg/m^3}$ is vapor density, and $A=6\times10^4\,\mathrm{m^2}$ is the area of horizontal cross section of discharge zone, which is assumed to equal the area of the vent field. In the meantime, the chlorinity signals are advected at the speed of interstitial flows, which is related to $\bar{w}_T$ as

$$\bar{w}_S=\frac{\bar{w}_T}{\phi}, \tag{B4}$$

where $\phi$ is crustal porosity.

Under tidal loading, the temperature, chlorinity, and the advection speeds can be written as

$$T_v=\bar{T}_v+\hat{T}_v, \tag{B5}$$

$$S_v=\bar{S}_v+\hat{S}_v, \tag{B6}$$

$$w_T=\bar{w}_T+\hat{w}_T, \tag{B7}$$

$$w_S=\bar{w}_S+\hat{w}_S, \tag{B8}$$

where the second terms on the right-hand sides represent tidally induced perturbations, which are assumed to be much smaller than the steady state terms. When neglecting adiabatic cooling and the tidally induced perturbation in fluid density, the conservation of energy for the rising vapor along the discharge zone can be expressed as [*Jupp and Schultz*, 2004b]:

$$\frac{\partial}{\partial t}(\bar{T}_v+\hat{T}_v)+(\bar{w}_T+\hat{w}_T)\frac{\partial}{\partial z}(\bar{T}_z+\hat{T}_z)=-\Gamma_T\bar{w}_T. \tag{B9}$$

Similarly, the conservation of chloride equation can be written as

$$\frac{\partial}{\partial t}(\bar{S}_v+\hat{S}_v)+(\bar{w}_S+\hat{w}_S)\frac{\partial}{\partial z}(\bar{S}_v+\hat{S}_v)=\Gamma_S\bar{w}_S. \tag{B10}$$

We linearize equations (B9) and (B10) by substituting (B1) and (B2) for $\bar{T}_v$ and $\bar{S}_v$ and neglecting the second-order perturbation terms to get

$$\frac{\partial\hat{T}_v}{\partial t}+\bar{w}_T\frac{\partial\hat{T}_v}{\partial z}=\Gamma_T\hat{w}_T, \tag{B11}$$

$$\frac{\partial\hat{S}_v}{\partial t}+\bar{w}_S\frac{\partial\hat{S}_v}{\partial z}=-\Gamma_S\hat{w}_S. \tag{B12}$$

The advection speed perturbation for temperature is related to the tidally induced incremental pore pressure by Darcy's law:

$$\hat{w}_T=-\frac{k}{\mu}\frac{\partial\hat{P}_d}{\partial z}. \tag{B13}$$

Again, since the chloride signals are advected at the speed of interstitial flows, we have

$$\hat{w}_S=\frac{1}{\phi}\hat{w}_T. \tag{B14}$$

Substituting equations (A9) and (A11) into (B13) gives

$$\hat{w}_{Tj}=-\frac{k_j}{\mu_j}[a_j\Psi_j\exp(\Psi_j z)-b_j\Psi_j\exp(-\Psi_j z)]\exp(i\Omega t), \tag{B15}$$

and from equation (B14):

$$\hat{w}_{Sj}=-\frac{k_j}{\mu_j\phi_j}[a_j\Psi_j\exp(\Psi_j z)-b_2\Psi_j\exp(-\Psi_j z)]\exp(i\Omega t). \tag{B16}$$

where subscript $j$ denotes properties in layer 2A: $j=1$ and layer 2B: $j=2$.

In practice, we substitute equations (B3) and (B4) for $\bar{w}_T$ and $\bar{w}_S$, equations (B15) and (B16) for $\hat{w}_T$ and $\hat{w}_S$ in equations (B11) and (B12). We then solve these two equations for $\hat{T}_v$ and $\hat{S}_v$ with the boundary conditions: $\hat{T}_v=\hat{S}_v=0$ at the bottom boundary of layer 2B ($z=-H=-2300$ m). Those boundary conditions are derived based on the assumption that the end-member vapor formed within the basal reaction zone has sufficient thermal and compositional inertia that the temperature and chlorinity are held constant under tidal loading. At layer 2A/2B interface, we assume continuity for temperature and chlorinity, which requires: $\hat{T}_{v1}=\hat{T}_{v2}$ and $\hat{S}_{v1}=\hat{S}_{v2}$ at $z=-h=-500$ m.

The solution to equations (B11) and (B12) have the following expressions:

$$\hat{T}_{vj}=\left\{q_{Tj}\exp\left(-\frac{i\Omega}{\bar{w}_{Tj}}z\right)+m_{Tj}\exp(\Psi_j z)+n_{Tj}\exp(-\Psi_j z)\right\}\exp(i\Omega t), \tag{B17}$$

$$\hat{S}_{vj}=\left\{q_{Sj}\exp\left(-\frac{i\Omega}{\bar{w}_{Sj}}z\right)+m_{Sj}\exp\left(\Psi_2 z\right)+n_{Sj}\exp\left(-\Psi_2 z\right)\right\}\exp\left(i\Omega t\right). \tag{B18}$$

The constant coefficients in equations (B17) and (B18) are:

$$m_{Tj}=-\frac{\Gamma_T k_j a_j \Psi_j}{\mu_j(\bar{w}_{Tj}\Psi_j+i\Omega)}, \tag{B19}$$

$$n_{Tj}=-\frac{\Gamma_T k_j b_j \Psi_j}{\mu_j(\bar{w}_{Tj}\Psi_j-i\Omega)}, \tag{B20}$$

$$q_{T2}=\frac{\left[-m_{T2}\exp\left(-\Psi_2 H\right)-n_{T2}\exp\left(\Psi_2 H\right)\right]}{\exp\left(i\Omega H/\bar{w}_{T2}\right)}, \tag{B21}$$

$$q_{T1}=\frac{\left[\frac{\hat{T}_{v2}|_{z=-h}}{\exp(i\Omega t)}-m_{T1}\exp\left(-\Psi_1 h\right)-n_{T1}\exp\left(\Psi_1 h\right)\right]}{\exp\left(i\Omega h/\bar{w}_{T1}\right)}, \tag{B22}$$

$$m_{Sj}=\frac{\Gamma_S k_j a_j \Psi_j}{\mu_j(\bar{w}_{Sj}\Psi_j+i\Omega)}, \tag{B23}$$

$$n_{Sj}=\frac{\Gamma_S k_j b_j \Psi_j}{\mu_j(\bar{w}_{Sj}\Psi_j-i\Omega)}, \tag{B24}$$

$$q_{S1}=\frac{\left[\frac{\hat{S}_{v2}|_{z=-h}}{\exp(i\Omega t)}-m_{S1}\exp\left(-\Psi_1 h\right)-n_{S1}\exp\left(\Psi_1 h\right)\right]}{\exp\left(i\Omega h/\bar{w}_{S1}\right)}, \tag{B25}$$

$$q_{S2}=\frac{\left[-m_{S2}\exp\left(-\Psi_2 H\right)-n_{S2}\exp\left(\Psi_2 H\right)\right]}{\exp\left(i\Omega H/\bar{w}_{S2}\right)}, \tag{B26}$$

where $a_j$ and $b_j$ are the constant coefficients in the solution of the diffusive pore pressure perturbation ($\hat{P}_d$) (equation (A11)).

**Acknowledgments**

G. Xu was funded by the Woods Hole Oceanographic Institution as a postdoctoral scholar. B. I. Larson was partially funded by the PMEL Earth-Ocean Interactions Program and the Joint Institute for the Study of the Atmosphere and Ocean (JISAO) under NOAA Cooperative agreement NA10OAR4320148. This is JISAO contribution 2016-01-33, and PMEL contribution 4533. K. G. Bemis was funded by the National Science Foundation (NSF) award OCE-1234141. The original development of the resistivity instruments was through an NSF grant to M. Lilley (94069965). Additional NSF grants (9820105, 0120392, 0701196, 0751868, and 0819004) allowed improvements and field deployments to be made. Additional support from the W. M. Keck Foundation is gratefully acknowledged. Funds to refurbish the instrument for the deployment that produced the data discussed here were provided by ONC. We gratefully acknowledge the ROPOS group along with Ian Kulin and Steve Mihaly for their efforts during the deployment. We also gratefully acknowledge the efforts of Eric Olson through many years to help make these instruments field ready. The temperature and resistivity data recorded by BARS can be downloaded through the data search interface of ONC database (http://dmas.uvic.ca/DataSearch).

## References

Barreyre, T., and R. A. Sohn (2016), Poroelastic response of mid-ocean ridge hydrothermal systems to ocean tidal loading: Implications for shallow permeability structure, *Geophys. Res. Lett.*, *43*, 1660–1668, doi:10.1002/2015GL066479.

Barreyre, T., J. Escartin, R. Sohn, and M. Cannat (2014a), Permeability of the lucky strike deep-sea hydrothermal system: Constraints from the poroelastic response to ocean tidal loading, *Earth Planet. Sci. Lett.*, *408*, 146–154, doi:10.1016/j.epsl.2014.09.049.

Barreyre, T., J. Escartín, R. A. Sohn, M. Cannat, V. Ballu, and W. C. Crawford (2014b), Temporal variability and tidal modulation of hydrothermal exit-fluid temperatures at the lucky strike deep-sea vent field, mid-Atlantic ridge, *J. Geophys. Res.*, *119*, 2543–2566, doi:10.1002/2013JB010478.

Carlson, R. L. (2011), The effect of hydrothermal alteration on the seismic structure of the upper oceanic crust: Evidence from holes 504b and 1256d, *Geochem. Geophys. Geosyst.*, *12*, Q09013, doi:10.1029/2011GC003624.

Choi, J., and R. P. Lowell (2015), The response of two-phase hydrothermal systems to changing magmatic heat input at mid-ocean ridges, *Deep Sea Res., Part II*, *121*, 17–30.

Clague, D. A., D. W. Caress, H. Thomas, D. Thompson, M. Calarco, J. Holden, and D. Butterfield (2008), Abundance and distribution of hydrothermal chimneys and mounds on the Endeavour Ridge determined by 1-m resolution AUV multibeam mapping surveys, *EOS Trans. AGU*, *89*(23), Fall Meet. Suppl., Abstract V41B-2079.

Clague, D. A., et al. (2014), Eruptive and tectonic history of the Endeavour Segment, Juan de Fuca Ridge, based on AUV mapping data and lava flow ages, *Geochem. Geophys. Geosyst.*, *15*, 3364–3391, doi:10.1002/2014GC005415.

Coogan, L. A. (2008), Reconciling temperatures of metamorphism, fluid fluxes, and heat transport in the upper crust at intermediate to fast spreading mid-ocean ridges, *Geochem. Geophys. Geosyst.*, *9*, Q02013, doi:10.1029/2007GC001787.

Coumou, D., T. Driesner, P. Weis, and C. A. Heinrich (2009), Phase separation, brine formation, and salinity variation at black smoker hydrothermal systems, *J. Geophys. Res.*, *114*, B03212, doi:10.1029/2008JB005764.

Crone, T. J., and W. S. D. Wilcock (2005), Modeling the effects of tidal loading on mid-ocean ridge hydrothermal systems, *Geochem. Geophys. Geosyst.*, *6*, Q07001, doi:10.1029/2004GC000905.

Crone, T. J., W. S. D. Wilcock, and R. E. McDuff (2010), Flow rate perturbations in a black smoker hydrothermal vent in response to a mid-ocean ridge earthquake swarm, *Geochem. Geophys. Geosyst.*, *11*, Q03012, doi:10.1029/2009GC002926.

Davis, E. E., K. Wang, K. Becker, and R. E. Thomson (2000), Formation-scale hydraulic and mechanical properties of oceanic crust inferred from pore pressure response to periodic seafloor loading, *J. Geophys. Res.*, *105*(B6), 13,423–13,435, doi:10.1029/2000JB900084.

Davis, E. E., K. Wang, R. E. Thomson, K. Becker, and J. F. Cassidy (2001), An episode of seafloor spreading and associated plate deformation inferred from crustal fluid pressure transients, *J. Geophys. Res.*, *106*(B10), 21,953–21,963, doi:10.1029/2000JB000040.

Driesner, T. (2007), The system H2O—NaCl. Part II: Correlations for molar volume, enthalpy, and isobaric heat capacity from 0 to 1000 °C, 1 to 5000 bar, and 0 to 1 $X_{NaCl}$, *Geochim. Cosmochim. Acta*, *71*, 4902–4919, doi:10.1016/j.gca.2006.01.033.

Driesner, T., and C. A. Heinrich (2007), The system H2O—NaCl. Part I: Correlation formulae for phase relations in temperature-pressure-composition space from 0 to 1000 °C, 0 to 5000 bar, and 0 to 1 $X_{NaCl}$, *Geochim. Cosmochim. Acta*, *71*, 4880–4901, doi:10.1016/j.gca.2006.01.033.

Fontaine, F. J., and W. S. D. Wilcock (2006), Dynamics and storage of brine in mid-ocean ridge hydrothermal systems, *J. Geophys. Res.*, *111*, B06102, doi:10.1029/2005JB003866.

Germanovich, L. N., R. P. Lowell, and D. K. Astakhov (2000), Stress-dependent permeability and the formation of seafloor event plumes, *J. Geophys. Res.*, *105*(B4), 8341–8354, doi:10.1029/1999JB900431.

Hearn, C. K., K. L. Homola, and H. P. Johnson (2013), Surficial permeability of the axial valley seafloor: Endeavour segment, Juan de Fuca ridge, *Geochem. Geophys. Geosyst.*, *14*, 3409–3424, doi:10.1002/ggge.20209.

Johnson, J. W., and D. Norton (1991), Critical phenomena in hydrothermal systems: State, thermodynamic, electrostatic, and transport properties of $H_2O$ in the critical region, *Am. J. Sci.*, *291*, 541–648, doi:10.2475/ajs.291.6.541.

Jupp, T. E., and A. Schultz (2000), A thermodynamic explanation for black smoker temperatures, *Nature*, *403*, 880–883, doi:10.1038/35002552.

Jupp, T. E., and A. Schultz (2004a), Physical balances in subseafloor hydrothermal convection cells, *J. Geophys. Res.*, *109*, B05101, doi:10.1029/2003JB002697.

Jupp, T. E., and A. Schultz (2004b), A poroelastic model for the tidal modulation of seafloor hydrothermal systems, *J. Geophys. Res.*, *109*, B03105, doi:10.1029/2003JB002583.

Kelley, D. S., J. R. Delaney, and S. Kim Juniper (2014), Establishing a new era of submarine volcanic observatories: Cabling Axial Seamount and the Endeavour Segment of the Juan de Fuca Ridge, *Mar. Geol.*, *352*, 426–450.

Klyukin, Y., T. Driesner, M. Steele-MacInnis, R. Lowell, and R. J. Bodnar (2016), Effect of salinity on mass and energy transport by hydrothermal fluids based on the physical and thermodynamic properties of h2o-nacl, *Geofluids*, *16*, 585–603, doi:10.1111/gfl.12181.

Larson, B. I. (2008), Watching the world sweat: Development and utilization of an in-situ conductivity sensor for monitoring chloride dynamics in high temperature hydrothermal fluids at divergent plate boundaries, PhD thesis, Univ. of Wash., Seattle.

Larson, B. I., E. J. Olson, and M. D. Lilley (2007), In situ measurement of dissolved chloride in high temperature hydrothermal fluids, *Geochim. Cosmochim. Acta*, *71*, 2510–2523, doi:10.1016/j.gca.2007.02.013.

Larson, B. I., M. D. Lilley, and E. J. Olson (2009), Parameters of subsurface brines and hydrothermal processes 12-15 months after the 1999 magmatic event at the Main Endeavor Field as inferred from in situ time series measurements of chloride and temperature, *J. Geophys. Res.*, *114*, B01207, doi:10.1029/2008JB005627.

Little, S. A., K. D. Stolzenbach, and F. J. Grassle (1988), Tidal current effects on temperature in diffuse hydrothermal flow: Guaymas basin, *Geophys. Res. Lett.*, *15*(13), 1491–1494.

Lowell, R. P., A. Farough, J. Hoover, and K. Cummings (2013), Characteristics of magma-driven hydrothermal systems at oceanic spreading centers, *Geochem. Geophys. Geosyst.*, *14*, 1756–1770, doi:10.1002/ggge.20109.

Nedimovi, M. R., S. M. Carbotte, J. B. Diebold, A. J. Harding, J. P. Canales, and G. M. Kent (2008), Upper crustal evolution across the Juan de Fuca ridge flanks, *Geochem. Geophys. Geosyst.*, *9*, Q09006, doi:10.1029/2008GC002085.

Nees, H. A., R. A. Lutz, T. M. Shank, and G. W. Luther III (2009), Pre- and post-eruption diffuse flow variability among tubeworm habitats at 950 north on the east pacific rise, *Deep Sea Res., Part II*, *56*(19–20), 1607–1615, doi:10.1016/j.dsr2.2009.05.007.

Newman, K. R., M. R. Nedimovi, J. P. Canales, and S. M. Carbotte (2011), Evolution of seismic layer 2b across the Juan de Fuca ridge from hydrophone streamer 2-d traveltime tomography, *Geochem. Geophys. Geosyst.*, *12*, Q05009, doi:10.1029/2010GC003462.

Ocean Networks Canada Data Archive (2014a), *BARS Resistivity Data From 1 Oct 2010 to 10 Feb 2014*, Univ. of Victoria, Victoria, B. C., Canada.

Ocean Networks Canada Data Archive (2014b), *BARS Temperature Data From 1 Oct 2010 to 10 Feb 2014*, Univ. of Victoria, Victoria, B. C., Canada. [Available at http://www.oceannetworks.ca.]

Pawlowicz, R., B. Beardsley, and S. Lentz (2002), Classical tidal harmonic analysis including error estimates in MATLAB using T-TIDE, *Comput. Geosci.*, *28*, 929–937.

Percival, D. B., and A. T. Walden (1993), *Spectral Analysis for Physical Applications*, Cambridge Univ. Press, Cambridge, U. K.

Scheirer, D. S., T. M. Shank, and D. J. Fornari (2006), Temperature variations at diffuse and focused flow hydrothermal vent sites along the northern east pacific rise, *Geochem. Geophys. Geosyst.*, *7*, Q03002, doi:10.1029/2005GC001094.

Schultz, A., P. Dickson, and H. Elderfield (1996), Temporal variations in diffuse hydrothermal flow at TAG, *Geophys. Res. Lett.*, *23*(23), 3471–3474, doi:10.1029/96GL02081.

Sohn, R. A., D. J. Fornari, K. L. V. Damm, J. A. Hildebrand, and S. C. Webb (1998), Seismic and hydrothermal evidence for a cracking event on the East Pacific Rise crest at 9 degrees 50 ′ N, *Nature*, *396*(6707), 159–161, doi:10.1038/24146.

Thomson, D. J. (1982), Spectrum estimation and harmonic analysis, *IEEE Proc.*, *70*(9), 1055–1096, doi:10.1109/PROC.1982.12433.

Tivey, M. K., A. M. Bradley, T. M. Joyce, and D. Kadko (2002), Insights into tide-related variability at seafloor hydrothermal vents from time-series temperature measurements, *Earth Planet. Sci. Lett.*, *202*, 693–707.

Van Ark, E. M., et al. (2007), Seismic structure of the Endeavour segment, Juan de Fuca ridge: Correlations with seismicity and hydrothermal activity, *J. Geophys. Res.*, *112*, B02401, doi:10.1029/2005JB004210.

Wang, K., and E. E. Davis (1996), Theory for the propagation of tidally induced pore pressure variations in layered subseafloor formations, *J. Geophys. Res.*, *101*(B5), 11,483–11,495, doi:10.1029/96JB00641.

Wilcock, W. S., and A. McNabb (1996), Estimates of crustal permeability on the endeavour segment of the Juan de Fuca mid-ocean ridge, *Earth Planet. Sci. Lett.*, *138*(1–4), 83–91, doi:10.1016/0012-821X(95)00225-2.